VISUALIZATION AND CHARACTERIZATION OF GRAVITY CURRENTS OVER ROUGH BEDS BY MEANS OF PIV MEASUREMENTS

Helena I. S. Nogueira[1], Claudia Adduce[2], Elsa Alves[3] & Mário J. Franca[4]

[1]Department of Civil Engineering & IMAR-CMA, University of Coimbra, Portugal, Rua Luís Reis Santos – Pólo II, 3030-788 Coimbra

[2]Department of Civil Engineering, University of "Roma Tre", Italy, Via Vito Volterra 62, 00146 Rome

[3]National Laboratory of Civil Engineering, Portugal, Avenida do Brasil 101, 1700-066 Lisbon

[4]Department of Civil Engineering & IMAR-CMA, New University of Lisbon, Portugal, Quinta da Torre, 2829-516 Caparica

E-mail: hnogueira@dec.uc.pt

Abstract

Particle Image Velocimetry (PIV) is herein used to investigate the influence of the bed roughness in the development of unsteady gravity currents, namely in what concerns the instantaneous two-dimensional velocity and vorticity fields. Density currents are performed by lock-release of a fixed volume of saline water into a fresh water tank. The experiments were conducted in a 3.0 m long Perspex flume of horizontal bed and rectangular cross section of 0.20×0.30 m^2. Four experiments were performed by varying the bed roughness maintaining the initial density of the saline water in the lock, the lock length and the water depth. The analysis of instantaneous velocity and vorticity maps obtained in the vertical centreline plane of the channel show that bed roughness reduces the overall streamwise velocity within the current and confers a vertically homogenized velocity distribution, therefore reducing the vorticity magnitude.

Introduction

Gravity currents encompass a wide range of flows driven by density differences which can be due to temperature, dissolved substances or particles in suspension. Although these currents are a major issue in geophysics, they are also important in engineering sciences, namely in industrial safety and environmental protection. The releases of pollutant materials into rivers, oil spillage on the sea environment, desalination plant outflows and industrial cooling systems outflow are a few of man-made density currents that occur in the water masses and frequently cause negative environmental impacts. The loss of storage in reservoirs, related to the deposition of fine sediments due to turbidity currents, is a subject of great concern to hydraulic engineers and still a topic of research nowadays (Kantoush et al. 2010; Rossato & Alves 2011). Several examples of natural and man-made gravity currents can be found comprehensively in Simpson (1997).

Gravity currents produced by lock-exchange technique present two, or even three, distinct phases (Rottman & Simpson 1983). After the gate removal, a slumping phase begins where the front of the current advances at approximately constant velocity; when the reflected bore, generated by the gate removal, overtakes the current front, an inertia-buoyancy phase takes place in which the front velocity decreases with time; when viscous effects start to dominate inertial effects, a viscous phase develops and the front velocity decreases even more rapidly.

Recent advances in measurement techniques have enabled velocity and density measurements within gravity currents. Several studies have been developed using Particle Image Velocimetry (Alahyari & Longmire 1996, Zhu et al. 2006, Adduce et al. 2011). The combination of PIV with such other methods, as Laser-Induced Fluorescence (Martin & García 2009) and PIV-S (Ramaprabhu & Andrews 2003, Gerber et al. 2011), allows the measurement of velocity and density simultaneously.

Alahyari & Longmire (1996) used PIV to investigate the dynamics of the head of axisymmetric gravity currents in the inertia-buoyancy phase of the flow. Instantaneous and ensemble-averaged 2D velocity maps show the existence of two counter-rotating large-scale vortices at the current head.

Kneller et al. (1999) studied the velocity structure and turbulence within gravity currents performed by lock-exchange experiments. They used Laser-Doppler Anemometry (LDA) to measure the instantaneous 2D flow velocity of currents in the slumping phase. The time-averaged vertical profiles of the streamwise velocity in the current body show a maximum at a height $z/d = 0.2$, where d is the current depth, and its magnitude is over 50% grater that the front velocity. Two regions inside the current were distinguished based on opposite vertical gradients of streamwise velocity. The authors argued that the mean motion within the current head is ruled by a single large vortex.

Thomas et al. (2003) used Particle-Tracking Velocimetry (PTV) to study gravity currents during the slumping phase. Based on time-averaged velocity fields they observed a different internal pattern of the flow from that reported by Kneller et al. (1999), namely the existence of two counter-rotating cells in the current head instead of one.

Peters & Venart (2000) used Laser-Induced Fluorescence (LIF) to investigate flow dynamics and mixing processes of gravity currents in the head region over rough surfaces. They used regular square cross-section elements spanning the full channel width with four different side dimensions to produce bed roughness. In general, they observed that roughness decreases the front velocity and induces higher dilution in the head region.

The main contributions herein cited generally concern flows developing over smooth surfaces. To our knowledge, the effect of the bed roughness in the structure of the velocity and vorticity within gravity currents has not yet been totally explored. Therefore, the present work aims visualizing and characterizing the effect of bed roughness on the velocity and vorticity pattern within gravity currents, namely in the head region, during the inertia-buoyancy phase of development through PIV measurements.

Experimental procedure

The experiments were performed at the Hydraulics Laboratory of University of Rome, "Roma Tre", in a 3.0 m long Perspex flume of horizontal bed and rectangular cross section of 0.20 x 0.30 m^2 (Figure 1). A saline mixture of initial density ρ_1 = 1015 kgm^{-3} is placed in a lock with a vertical sliding gate at a distance x_0 = 0.15 m from the upstream section, i.e., left wall of the channel. The right side of the channel is filled with fresh water with density ρ_0 = 1000 kgm^{-3}, both sides filled up at same depth, h_0 = 0.2 m. The experiment begins when the gate is totally removed leading the dense fluid to flow under the fresh water.

The laser source of the PIV system (Intelligent Laser Applications) was placed at the right end wall of the channel, being the laser sheet adjusted to illuminate the vertical centreline plane of the channel. A CCD camera (PCO Pixelfly^{TM} double shutter with 1392 x 1024 pixels of resolution) was kept at a fixed perpendicular position to the sidewall capturing a field of view of 0.33 m long and 0.18 m deep, starting from x = 1.5 m, as shown schematically in Figure 1. The back wall of the channel was lined with black paperboard to produce a uniform dark background. Temperature measurements were performed in the fresh water inside the channel to control its density before the beginning of each experiment.

Four experiments were performed by changing the roughness of the bed, maintaining constant all the other variables, leading to the following runs: D1, ε = 0 mm (smooth bed); R1, ε = 2.9 mm; R2, ε = 4.6 mm and R3, ε = 24.6 mm.

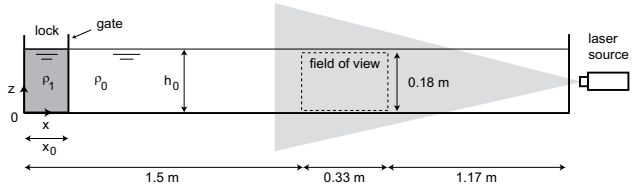

Figure 1. Schematic view of experimental set-up.

Figure 2. Details of the rough beds used for runs of type R: R1 (left), R2 (center) and R3 (right). View of the channel bed from the downstream section, i.e., right end wall.

The sediment disposal in the channel was made layer by layer, until reaching a total thickness around $3D_{50}$, where D_{50} is the grain size diameter for which 50% of the sediments have smaller diameters, herein the same meaning as roughness ε. The water depth h_0 in the rough bed experiments was measured from the top of the sediment layer.

A double pulsed Nd:YAG laser was used to measure the 2D instantaneous flow velocity, being the pair of images acquired at 3 Hz with 30 ms between pulses. Both dense fluid and ambient fluid were seeded with polyamide particles with a mean diameter of 100 μm and mean density of 1016 kgm^{-3}. Regarding data analysis, the velocity interrogation areas had a size of 64 x 64 pixels, reduced to 32 x 32 pixels with a 50% overlap, resulting in a 4 x 4 mm^2 grid of velocity vectors.

The vorticity component perpendicular to the measurement plane is defined by:

$$\eta = \frac{\partial w}{\partial x} - \frac{\partial u}{\partial z} \tag{1}$$

where u and w are the streamwise and vertical components of the velocity, respectively. The algorithm used to estimate (1) is proposed by Sveen (2004):

$$\left.\frac{\partial w}{\partial x}\right|_{i,j} = \frac{2w_{i,j+2} + w_{i,j+1} - w_{i,j-1} - 2w_{i,j-2}}{10\Delta x} \tag{2}$$

$$\left.\frac{\partial u}{\partial z}\right|_{i,j} = \frac{2u_{i+2,j} + u_{i+1,j} - u_{i-1,j} - 2u_{i-2,j}}{10\Delta z} \tag{3}$$

where Δx and Δz are the distances in the streamwise and vertical directions between adjacent measuring points,

respectively. Velocity and vorticity maps are presented for the instant when the current front reaches the downstream limit of the visualization area. The time after the gate release is non-dimensionalized by the following time scale:

$$t_0 = \frac{x_0}{\sqrt{g' h_0}} \quad (4)$$

where $g' = g\Delta\rho/\rho_0$ is the reduced gravity and $\Delta\rho$ is the density difference between the saline mixture and the ambient fluid. Flow depth is normalized by the initial depth at the lock, h_0, and streamwise distance is represented in terms of lock-lengths, $(x\text{-}x_0)/x_0$.

Results

Velocity maps

Figure 3 shows the vector maps of the instantaneous velocity field superimposed on the instantaneous streamwise velocity distribution for all runs performed.

In general, as the bed roughness increases, lower streamwise velocity is observed within the current as a result of the additional bed drag. Besides current deceleration, bed roughness seems to induce a homogenizing effect in the distribution of the streamwise velocity.

Figure 3, run D1, shows two regions of maximum streamwise velocity below the upper mixing layer at $(x\text{-}x_0)/x_0 = 9.5$ and 10.2. As velocity vectors suggest, these regions are located under two large-scale rotating cells which push forward the flow, leading to $u_{max} \approx 9$ cms^{-1}, substantially superior to the front velocity, $u_f \approx 7$ cms^{-1} (cf. Nogueira et al. 2011). By continuity, the ambient fluid above the rotating cells is pushed towards upstream with negative streamwise velocity around $u = 4$ cms^{-1}. The analysis of the following instants of the current development, not shown here, show that these rotating cells persist in time, being slightly dragged towards downstream by the mean flow of the current.

In the runs performed over rough beds, although a homogenizing effect is observed in the distribution of the u-component, there are regions with high streamwise velocity within the current, curiously located at similar positions between runs, around $(x\text{-}x_0)/x_0 = 9.8$ to 10.1. In general, these regions are located nearer the flow bed extending over a wider area in the vertical direction, when comparing with the smooth bed case (cf. vertical profiles in Figure 4). In terms of magnitude, the maximum of streamwise velocity is approximately 8 cms^{-1} in runs R1 and R2, decreasing to 6.5 cms^{-1} in run R3.

Vertical velocity profiles

Figures 4 and 5 show, respectively, the vertical profiles of the instantaneous streamwise and vertical components of the velocity taken at $(x\text{-}x_0)/x_0 = 9.3$, 10 and 10.7 (represented by the vertical dashed lines in Figure 3).

The u-component profiles show that the maximum value is always under $z/h_0 = 0.2$. In the smooth bed case, a trend in the peak location as a function of the streamwise position can be established: moving towards upstream, the u_{max} region starts to approach the flow bed, as an effect of the large-scale rotating cells visible in Figure 3.

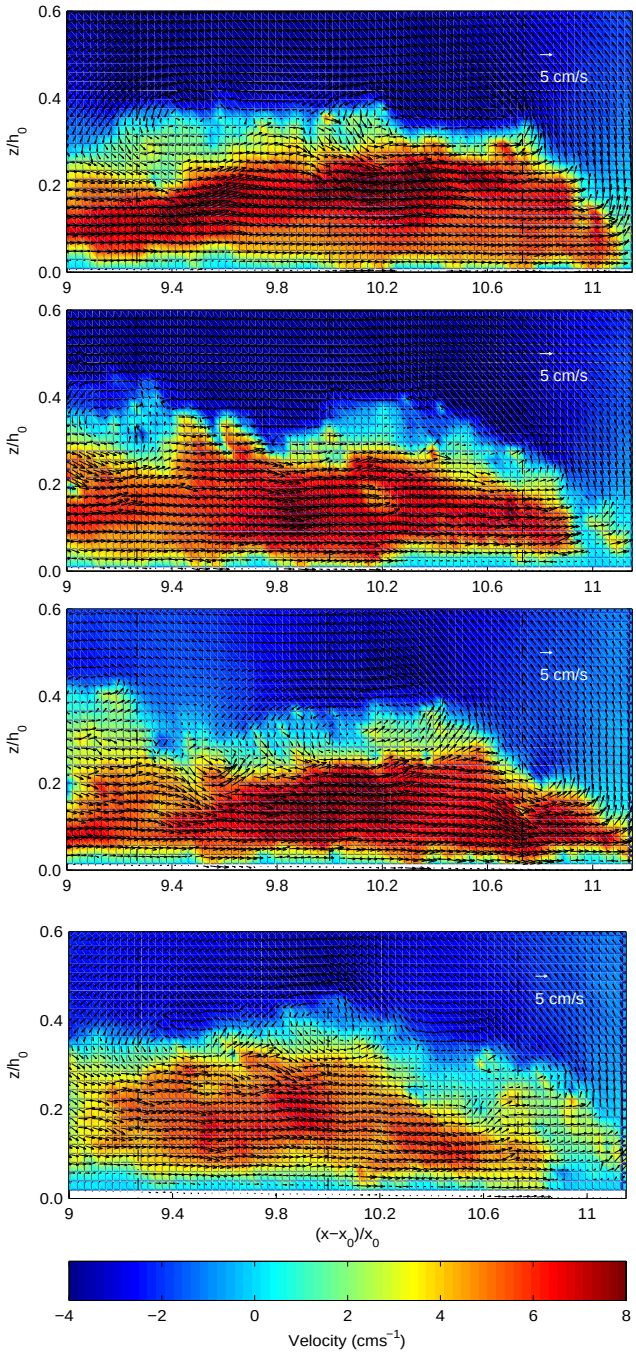

Figure 3. Vector maps of the instantaneous velocity field superimposed on the distribution of streamwise component u. From top to bottom: runs D1 ($t/t_0 = 23$), R1 ($t/t_0 = 23$), R2 ($t/t_0 = 25.7$), and R3 ($t/t_0 = 30.3$). Vertical dashed lines represent the location of the vertical profiles shown in Figures 4 and 5.

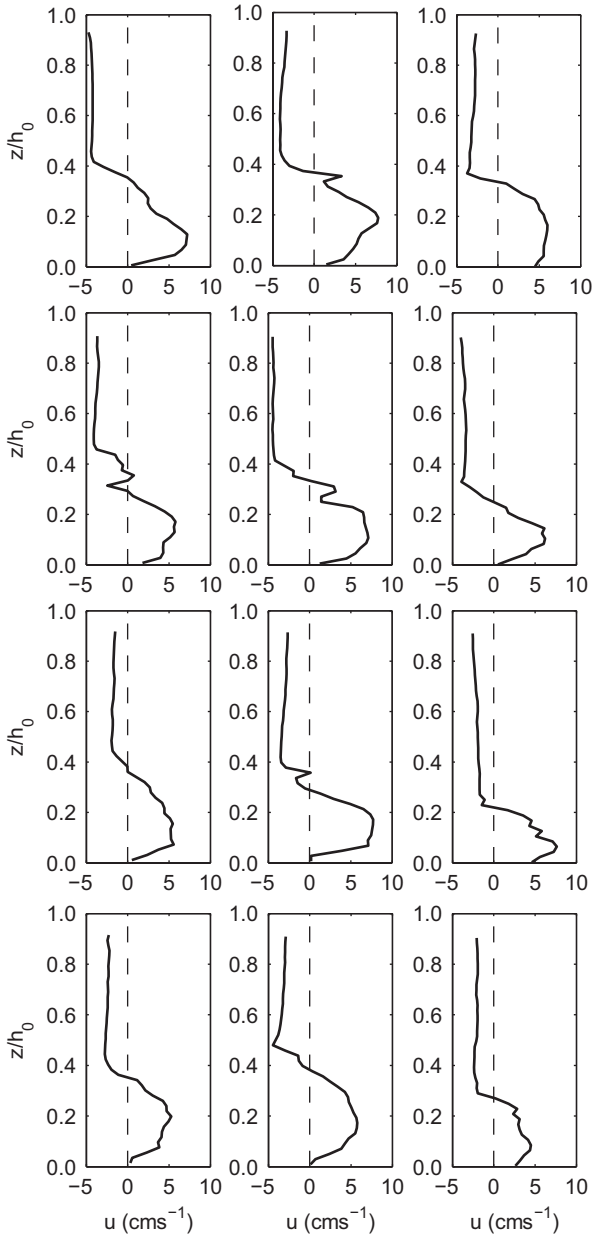

Figure 4. Vertical profiles of *u*-component acquired at $(x\text{-}x_0)/x_0$ = 9.3 (left), 10 (center) and 10.7 (right). From top to bottom: runs D1 (t/t_0 = 23), R1 (t/t_0 = 23), R2 (t/t_0 = 25.7), and R3 (t/t_0 = 30.3).

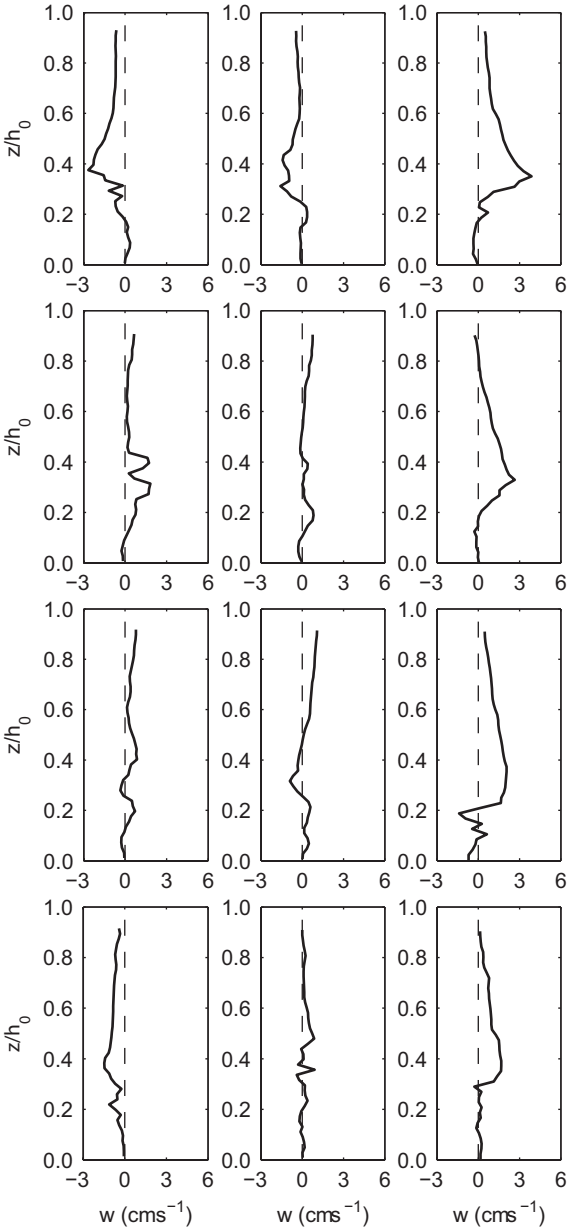

Figure 5. Vertical profiles of *w*-component acquired at $(x\text{-}x_0)/x_0$ = 9.3 (left), 10 (center) and 10.7 (right). From top to bottom: runs D1 (t/t_0 = 23), R1 (t/t_0 = 23), R2 (t/t_0 = 25.7), and R3 (t/t_0 = 30.3).

The *w*-component profiles show that an important region of positive velocity (upward) is located in the frontal interface between fluids, where w_{max} reaches 4 cms^{-1} in the smooth bed case, representing roughly 50% of the maximum streamwise velocity. Similar observation can be stated for the rough bed runs. The region of negative vertical velocity (downwards) is in all cases associated with the rear of vortex structures present in the upper mixing layer (cf. Figure 3), causing ambient fluid to be entrained.

Vorticity maps

Figure 6 shows the vorticity distribution superimposed by the vector map of instantaneous velocity. Typically, the vorticity field shows a region of positive vorticity in the interface between the two fluids, arising from the shear between current and ambient fluid, while negative vorticity is observed near the flow bed as a result of the no-slip boundary condition. Increasing bed roughness reduces the overall vorticity magnitude, which was expected from the more homogenized distribution of the streamwise velocity in the vertical direction.

Figure 6, run D1, shows the region of high positive vorticity starting at the head of the current, distributed in a narrow stripe. This region extends towards upstream increasing its thickness and decreasing in intensity (similar to the observations of Thomas et al 2003 in time-averaged

vorticity maps). The two large-scale rotating cells identified earlier at $(x\text{-}x_0)/x_0$ = 9.5 and 10.2, correspond to signatures in the vorticity maps. The negative vorticity region has a maximum at $(x\text{-}x_0)/x_0$ = 9.4 near the flow bed.

Run R1 presents a more complex vorticity distribution, where the region of positive vorticity near the front has a wider thickness and lower intensity, when compared with the smooth bed case. The region of maximum positive vorticity is located at the rear of the head while the region of maximum negative vorticity is near the flow bed in the head region.

Run R2 exhibits a region of maximum vorticity near the front region, in a narrow stripe, similarly to what was observed in run D1.

Finally, run R3 shows a more diffuse distribution of vorticity, with lower magnitude, where two adjacent large-scale rotating cells can be identified in the upper mixing layer at $(x\text{-}x_0)/x_0$ = 9.4 to 10.1.

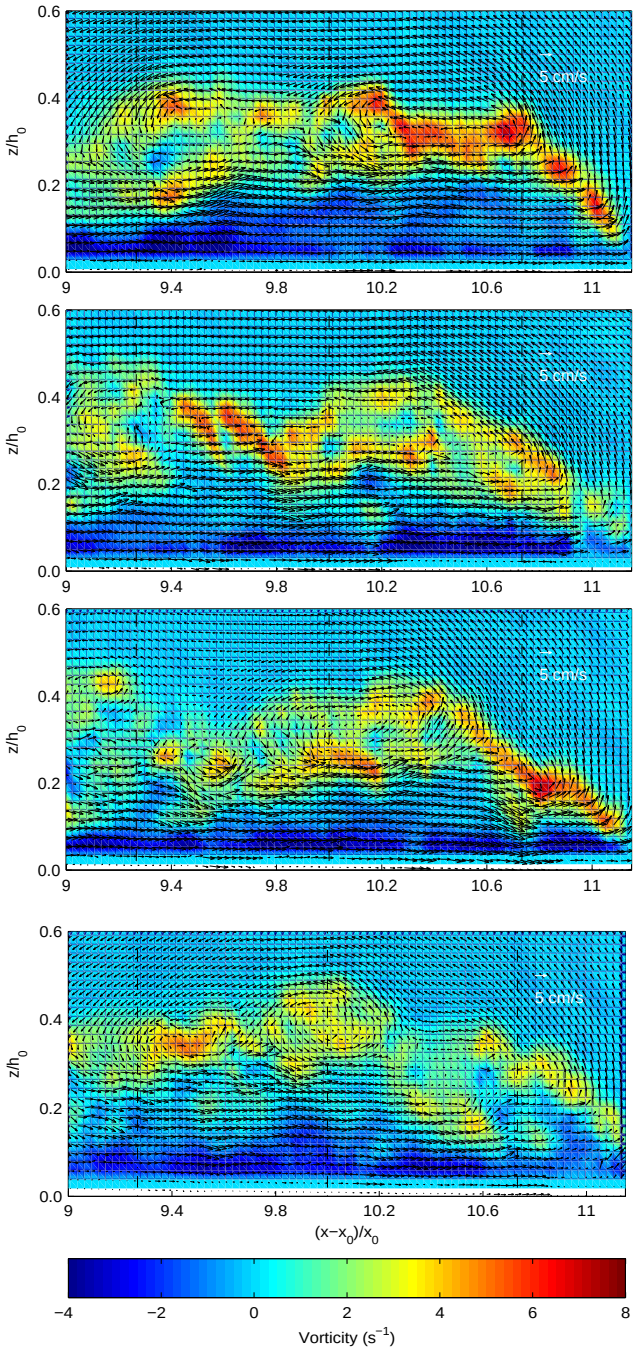

Figure 6. Instantaneous vorticity maps superimposed by instantaneous velocity vectors. From top to bottom: runs D1 (t/t_0 = 23), R1 (t/t_0 = 23), R2 (t/t_0 = 25.7), and R3 (t/t_0 = 30.3). Vertical dashed lines represent the location of the vertical profiles shown in Figure 7.

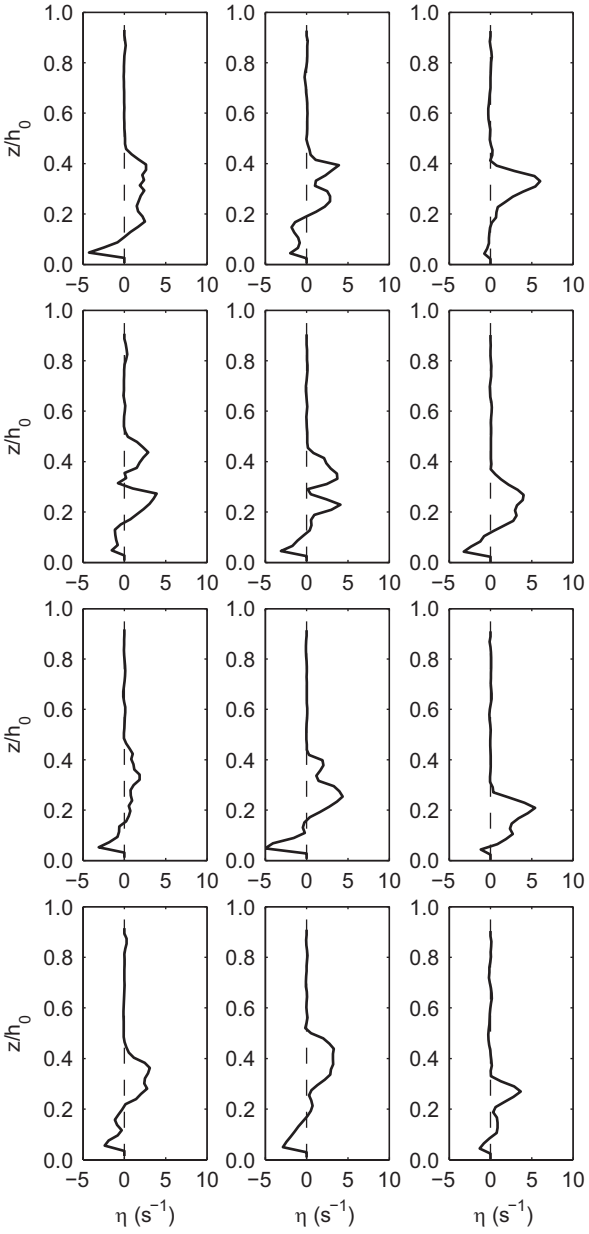

Figure 7. Vertical profiles of vorticity acquired at $(x\text{-}x_0)/x_0$ = 9.3 (left), 10 (center) and 10.7 (right). From top to bottom: runs D1 (t/t_0 = 23), R1 (t/t_0 = 23), R2 (t/t_0 = 25.7), and R3 (t/t_0 = 30.3).

Vertical vorticity profiles

Figure 7 shows the vertical profiles of the instantaneous vorticity taken at $(x\text{-}x_0)/x_0 = 9.3$, 10 and 10.7 (represented by vertical dashed lines in Figure 6).

These profiles show clearly two regions of opposite vorticity in all runs, as already observed in the instantaneous maps in Figure 6. The transition from positive to negative vorticity corresponds to the location of the streamwise velocity maxima, whose location was seen to be under $z/h_0 = 0.2$, varying slightly in the streamwise direction for all runs. The pattern of vorticity within the upper mixing layer is complex and characterized by one or two significant regions of maximum vorticity, corroborating the findings commented earlier in the text.

Conclusions

Particle Image Velocimetry was used to investigate the instantaneous structure of the head of lock-released gravity currents developing over smooth and rough beds at the inertia-buoyancy stage. The internal pattern of velocity and vorticity is rather complex.

The additional bed drag induced by rough elements is seen to reduce the overall streamwise velocity within the current and confers a vertically homogenized velocity distribution. The vertical component of the velocity is seen to be significant near the frontal interface between current and ambient fluid and within the upper mixing layer. It was observed that $w_{max} \approx 50\%\ u_{max}$, for all runs, including for the smooth bed case.

Regarding the instantaneous vorticity distribution, results herein presented show a reduction in the overall vorticity magnitude when increasing the bed roughness. This is intrinsically related to the reduction of streamwise velocity gradients.

We believe that the analysis of instantaneous velocity and vorticity maps is the most suitable method to investigate the inner structure of gravity currents, due to its internal complexity, which would be lost with ensemble or time-averaged analysis.

Acknowledgements

This research was supported by the Portuguese Science and Technology Foundation through the research project PTDC/ECM/099752/2008 and the research grant SFRH/BD/48705/2008.

References

Adduce, C., Lombardi, V., Sciortino, G. La Rocca, M. & Morganti, M. (2011). Analysis of lock release gravity currents by PIV. *Proc. 7th Int. Symp. on Stratified Flows*, Rome, 22-26 August 2011.

Alahyari, A. & Longmire E.K. (1996). Development and structure of a gravity current head. *Exp Fluids* 20:410–416.

Gerber, G., Diefericks, G. & Basson, R. (2011). Particle image velocimetry measurements and numerical modelling of a saline density current. *J Hydr Eng* 137(3):333-342.

Kantoush, S.A., Sumi, T. & Murasaki, M. (2010). Evaluation of sediment bypass efficiency by flow field and sediment concentration monitoring techniques. *Annual J Hydr Eng* 55.

Kneller, B.C., Bennet S.J. & McCaffrey, W.D. (1999). Velocity structure, turbulence and fluid stresses in experimental gravity currents. *J Geophys Res* 104(C3):5381–5391.

Martin, J.E. & García, M.H. (2009). Combined PIV/PLIF measurements of a steady density current front. *Exp Fluids* 46:265-276.

Nogueira, H.I.S., Adduce, C., Alves, E. & Franca, M.J. (2011). Phase analysis of lock-exchange gravity currents. *Proc. 7th Int. Symp. on Stratified Flows*, Rome, 22-26 August 2011.

Peters, W.D. & Venart, J.E.S. (2000). Visualization of rough-surface gravity current flows using laser-induced fluorescence. *Proc. 9th Int. Symp. of Flow Visualization*. Edinburgh, 2000.

Ramaprabhu, P. & Andrews, M. J. (2003). Simultaneous measurements of velocity and density in buoyancy-driven mixing. *Exp Fluids* 34(1):98-106.

Rossato, R. & Alves, E. (2011). Experimental study of turbidity currents flow around obstacles. *Proc. 7th Int. Symp. on Stratified Flows*. Rome, 22-26 August 2011.

Rottman, J.W. & Simpson, J.E. (1983). Gravity currents produced by instantaneous releases of a heavy fluid in a rectangular channel. *J Fluid Mech* 135:95-110.

Simpson, J.E. (1997). *Gravity currents: in the environment and the laboratory*. 2nd edn., Cambridge University Press, New York, pp 1-2.

Sveen, J. (2004). An Introduction to MatPIV v.1.6.1; University of Oslo, Norway.

Thomas, L.P., Dalziel, S.B. & Marino, B.M. (2003). The structure of the head of an inertial gravity current determined by particle-tracking velocimetry. *Exp Fluids* 34:708–716.

Zhu, J.B., Lee, C.B., Chen, G.Q. & Lee, J.H.W. (2006). PIV observation of instantaneous velocity structure of lock release gravity currents in the slumping phase. *Communications in Nonlinear Science & Numerical Simulations* 11:262-270.